Available online at www.sciencedirect.com
ScienceDirect
Journal of Computational Physics 221 (2007) 761–780
JOURNAL OF COMPUTATIONAL PHYSICS
www.elsevier.com/locate/jcp

A moving mesh interface tracking method for 3D incompressible two-phase flows

Shaoping Quan, David P. Schmidt *

Department of Mechanical and Industrial Engineering, The University of Massachusetts at Amherst, Engineering Laboratory, Amherst, MA 01003-2210, USA

Received 4 January 2006; received in revised form 7 June 2006; accepted 28 June 2006
Available online 21 August 2006

Abstract

An interface tracking method using an unstructured moving mesh has been developed for simulating three-dimensional, incompressible, and immiscible two-phase flows. The interface mesh is moved in a Lagrangian fashion. A local mesh adaptation method is used to capture the changing interface curvature, maintain good mesh quality, and deal with large deformation. The interface is of zero thickness, so the jump and continuity conditions across the interface are implemented directly, without any smoothing of the properties of the two fluids. This is theoretically beneficial compared to other methods that allow the fluids' properties to continuously vary in an interface region. The curvature for interfacial tension calculation is geometrically computed by a least squares parabola fitting method. A mesh separation scheme for interfacial flows is employed to handle topological transition. The numerical technique is tested and validated by several cases, which include a two-layer Couette flow, an oscillating droplet surrounded by gas, and a droplet in shear flow. The results obtained from numerical simulations are found to be in excellent agreement with analytical solutions and experimental results. A collapsing ligament in a quiescent gas flow and a modulated jet pinching are simulated to show the robustness of the method.

Keywords: Moving mesh; Interface tracking; Two-phase flows; Jump conditions; Mesh adaptation; Mesh separation; Geometric harmonic mean; Dynamic convergence criteria

1. Introduction

Multiphase flows are of great importance in nature and in engineering applications, but they are notoriously difficult to simulate because of the discontinuities across the moving and deforming interface. Numerical simulations of two-phase flows are especially useful for problems with very small length and time scales, where it is difficult to perform experimental measurements in detail, such as primary atomization in sprays.

* Corresponding author. Tel.: +1 413 545 1393; fax: +1 413 545 1027.
E-mail address: schmidt@ecs.umass.edu (D.P. Schmidt).

0021-9991/$ - see front matter
doi:10.1016/j.jcp.2006.06.044

There are two main approaches to simulating incompressible, immiscible multiphase flow. The first is the diffuse-interface method, which allows a finite thickness of the interface, and the second is the sharp-interface method, which treats the interface as a zero thickness surface. The volume of fluid (VOF) method [1], the level set method [2,3], and the front tracking method [4,5] are schemes in the diffusive-interface category. All these methods use a fixed grid to solve the governing Navier–Stokes equations with different approaches to locating the interface, which simplifies dealing with large deformation and changing topology. In the above methods, however, the jumps in the fluids' properties and surface tension are usually smoothed in an interface region. Furthermore, the interface is smeared in VOF, and the level set method has difficulties with mass conservation. However, the level set method can be used for sharp interfaces when combined with the immersed interface method [6–8]. The lattice Boltzmann method (LBM) was used by He et al. [9] and Inamuro et al. [10] to simulate multiphase fluid flows. The interface is tracked by an index function and has a thickness of 3–4 cell sizes. The surface tension is modeled by incorporating molecular interactions. LBM is an efficient algorithm for simulating multiphase flows [11]. However, the LBM method is difficult to generalize beyond its domain of validity and the jump conditions across the interface are not satisfied [1].

The boundary integral method (BIM) [12,13] is in the sharp-interface category. A boundary integral representation applies to fluid problems where the governing equations can be formed using Green's functions. The boundary integral method is good at accurately and efficiently capturing the interface dynamics, but it is difficult to apply to more general fluid flows with a finite Reynolds number. Another method that can also maintain a sharp interface is the interface tracking with moving mesh technique, which is the approach in this paper. The pioneering work was done by Welch [14] and Hu et al. [15]. Welch could only simulate small interface deformation due to lack of mesh adaptation schemes. In Hu et al.'s method, if any low quality mesh elements were detected, then a new mesh would be generated and the solution from the old mesh would be projected to the new mesh. Obviously, the error due to global projection would be significant.

Perot and Nallapati [16] and Dai et al. [17,18] used a moving unstructured staggered mesh method to simulate incompressible free-surface flow. A local mesh adaptation scheme was employed in their work to deal with mesh distortion. This paper extends Perot and Nallapati [16] and Dai et al.'s work [17,18] to two-phase flow simulations. The jump and continuity conditions across the interface are carefully handled to achieve accuracy and stability. Several new mesh adaptation schemes are employed to deal with interface deformation, and a mesh separation method for two-phase flows is introduced to deal with interface pinching. This paper is organized as follows: the governing equations and the jump conditions are given in Section 2, and the numerical schemes are presented in Section 3. The mesh adaptation methods are described in Section 4. The mesh separation scheme is given in Section 5. The method is validated and tested by a number of two-phase flow problems in Section 6. Conclusions are given in Section 7.

2. Governing equations and jump conditions

The governing equations for incompressible flow in a moving and deforming control volume are

$$\frac{\mathrm{d}}{\mathrm{d}t}\int\int_{CV}\int \mathrm{d}v = \int\int_{CS} \mathbf{v}\cdot\mathbf{n}\,\mathrm{d}s, \tag{1}$$

$$\frac{\mathrm{d}}{\mathrm{d}t}\int\int_{CV}\int \rho\,\mathrm{d}v + \int\int_{CS} \rho(\mathbf{u}-\mathbf{v})\cdot\mathbf{n}\,\mathrm{d}s = 0, \tag{2}$$

$$\frac{\mathrm{d}}{\mathrm{d}t}\int\int_{CV}\int \rho\mathbf{u}\,\mathrm{d}v + \int\int_{CS} \rho\mathbf{u}(\mathbf{u}-\mathbf{v})\cdot\mathbf{n}\,\mathrm{d}s = \int\int_{CV}\int \rho\mathbf{f}\,\mathrm{d}v - \int\int_{CS} p\cdot\mathbf{n}\,\mathrm{d}s + \int\int_{CS} \mu(\nabla\mathbf{u}+\nabla\mathbf{u}^{\mathrm{T}})\cdot\mathbf{n}\,\mathrm{d}s, \tag{3}$$

where CV is a control volume, CS stands for the surface of the control volume, $\mathbf{u}$ is the fluid velocity, $\mathbf{v}$ is the surface velocity of the control volume, $\mathbf{n}$ stands for the unit vector of the face normal, $\mathbf{f}$ denotes the body force per unit mass, and the superscript T stands for the transpose. Eq. (1) is a consistency requirement for a moving control volume, which indicates that the rate of volume change is equal to a closed control surface integral of $\mathbf{v}$.

Using conservation of mass and linear momentum while considering the surface tension, the continuity and jump conditions across the interface for incompressible and immiscible two-phase flows are

$$u_{1n} = u_{2n} = v_n, \tag{4}$$

$$[\![u_\tau]\!] = 0, \tag{5}$$

$$[\![p]\!] = -\sigma\left(\frac{1}{R_1} + \frac{1}{R_2}\right) + [\![2\mu(\nabla \mathbf{u} \cdot \mathbf{n}) \cdot \mathbf{n}]\!], \tag{6}$$

$$\left[\!\!\left[\mu\left(\frac{\partial u_i}{\partial x_j} + \frac{\partial u_j}{\partial x_i}\right)\tau_i n_j\right]\!\!\right] = 0, \tag{7}$$

where σ stands for the surface tension coefficient and is assumed to be a constant, R_1 and R_2 are the principle radii of the surface, τ denotes the tangential unit vector, and $[\![\,]\!]$ stands for the difference across the interface. Eq. (4) indicates that the normal velocities of the two fluids across the interface should be continuous and should be equal to the normal velocity of the moving mesh in order to conserve mass. Eq. (5) is the continuity of the tangential velocities across the interface due to no-slip boundary condition on the interface. So it can be concluded that the interface should move with the fluids' velocities in order to conserve mass and to satisfy the boundary condition on the interface. Furthermore, this indicates that the momentum flux across the interface is identically zero. Thus the present scheme tends to be robust with large density differences, since the two fluids never co-exist in the same cell. The jump in pressure should be balanced by the surface tension added to the jump in viscous normal stresses, which is illustrated in Eq. (6). Eq. (7) is the continuity of viscous shear stresses across the interface.

3. Numerical schemes

3.1. Discretization of governing equations

The numerical scheme solves a discrete stream function formulation of the Navier–Stokes equations where an exact fractional step method [19] is employed. By solving the governing equations in such a way, conservation of mass is satisfied automatically, and the solution of a Poisson equation for pressure can be avoided. A brief description of the scheme is given here, and the details of this method can be found in [16].

The governing Eqs. (1)–(3) are discretized as reported previously in [16]

$$\frac{V_c^{n+1} - V_c^n}{\Delta t} = \sum_{\text{cell faces}} U_f^{\text{mesh}}, \tag{8}$$

$$\frac{\rho_c^{n+1} V_c^{n+1} - \rho_c^n V_c^n}{\Delta t} + \sum_{\text{cell faces}} \rho_f (U_f - U_f^{\text{mesh}}) = 0, \tag{9}$$

$$\begin{aligned}\frac{\rho_c^{n+1}\mathbf{u}_c^{n+1} V_c^{n+1} - \rho_c^n \mathbf{u}_c^n V_c^n}{\Delta t} &+ \sum_{\text{cell faces}} \rho_f \mathbf{u}_f (U_f - U_f^{\text{mesh}}) \\ &= -V_c \nabla(p - \rho \mathbf{g} \cdot \mathbf{r}_c^{CG}) + \sum_{\text{cell faces}} \mu(\nabla \mathbf{u} + \nabla \mathbf{u}^T) \cdot \mathbf{n}_f A_f - V_c(\mathbf{g} \cdot \mathbf{r}_c^{CG}) \nabla \rho,\end{aligned} \tag{10}$$

where V_c denotes the cell volume, U_f is the face flux, U_f^{mesh} stands for the moving mesh flux of the face, $\mathbf{r}_c^{CG}$ denotes the position of the cell center of gravity, A_f is the face area, $\mathbf{g}$ stands for gravitational force per unit mass, the superscript n is time step, and the subscripts f and c denote the cell and the face respectively. The stream function vectors are defined at the edge centers, and using Stokes' theorem and Gauss' divergence theorem, U_f, and the cell center velocity $\mathbf{u}_c$, can be constructed from the stream function vector $\mathbf{s}$ by following equations:

$$U_f = \sum_{\text{face edges}} \mathbf{s} \cdot \mathbf{t} \Delta l, \tag{11}$$

$$\mathbf{u}_c = \frac{1}{V} \sum_{\text{cell faces}} \mathbf{r}_f^{CG} U_f, \tag{12}$$

where $\mathbf{t}$ is the edge tangential unit vector, Δl denotes the edge length, $\mathbf{r}_f^{CG}$ stands for the distance vector from the cell centroid to the face center, and $\mathbf{x}_f$ is the position vector of the face centroid.

The normal velocity of the mesh faces is required for conservation of momentum in a moving, deforming control volume, as indicated in Eq. (9). The value of U_f^{mesh} can be found from the displacement of the neighboring nodes [16]

$$U_f^{mesh} = \frac{\mathbf{x}_f^{n+1} - \mathbf{x}_f^n}{\Delta t} \cdot \left[\frac{1}{2}(\mathbf{n}_f^{n+1} A_f^{n+1} + \mathbf{n}_f^n A_f^n) - \frac{\Delta t^2}{12} \sum_{\text{face edges}} (\mathbf{v}_{n1} \times \mathbf{v}_{n2}) \right]. \tag{13}$$

3.2. Continuity in viscous shear stress

The viscous shear stresses across the interface should be continuous, while the viscosity on the interface is undefined. Tryggvason et al. [20] used the arithmetic average for the interface viscosity for the cases where the less viscous fluid is expected to have a small effect, and the harmonic mean otherwise. These two methods for interface viscosity interpolation are tested for a two-dimensional, two-layer Couette flow which is shown in Fig. 1. Here u is the interface cell velocity and assigned to the theoretical value, and L stands for the distance from interface cell center to the interface. For the case with viscosity ratio ($\lambda = \mu_1/\mu_2$) of 0.01 and $L_1 = L_2$, the arithmetic average method gives a relative error of the interface shear stresses of 2450%, while the harmonic mean method predicts an exact result. However, the harmonic mean method has the relative errors of 65% and -65% for $\lambda = 0.01, l = 5$ and $\lambda = 0.01, l = 0.2$ respectively. Here l is the distance ratio and is defined as $l = L_1/L_2$.

A new interpolation of the interface viscosity is proposed to improve the accuracy of the calculation of the interface shear stresses. The continuity of the shear stresses across the interface (Eq. (7)) is given by

$$\mu_1 \frac{u_1 - u_i}{L_1} = \mu_2 \frac{u_i - u_2}{L_2} = \tau_i \tag{14}$$

for the case in Fig. 1, where u_i is the interface velocity, u_1 and u_2 are the velocities at the cell centers of each phase, and they are assumed to be linear in space, and τ_i stands for the interface shear stress. By rearranging Eq. (14), the following expressions are obtained:

$$u_1 - u_i = \frac{\tau_i L_1}{\mu_1}, \tag{15}$$

$$u_i - u_2 = \frac{\tau_i L_2}{\mu_2}. \tag{16}$$

Adding the above two equations, the interface shear stress can be expressed as

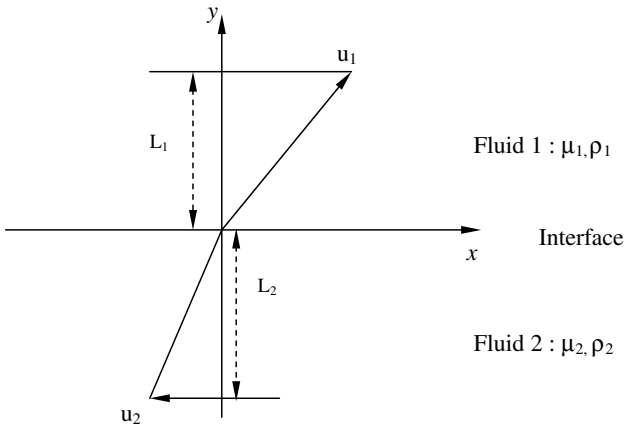

Fig. 1. Sketch of two-layer Couette flow. L_1 and L_2 are the distances from the cells' centers to the interface center. Vectors u_1 and u_2 denotes the cells' velocities.

$$\tau_i = \frac{u_1 - u_2}{\frac{L_1}{\mu_1} + \frac{L_2}{\mu_2}}. \tag{17}$$

Eq. (17) can be rewritten as

$$\tau_i = \frac{1}{\frac{\mathrm{d}x_1}{\mu_1} + \frac{\mathrm{d}x_2}{\mu_2}} \frac{u_1 - u_2}{L}, \tag{18}$$

where $L = L_1 + L_2$, $\mathrm{d}x_1 = L_1/L$, and $\mathrm{d}x_2 = L_2/L$. Since Eq. (18) predicts the exact interface shear stress for linear velocity distribution, it is second order accurate. Then the effective viscosity on the interface can be evaluated by

$$\mu_{i-\text{effective}} = \frac{1}{\frac{\mathrm{d}x_1}{\mu_1} + \frac{\mathrm{d}x_2}{\mu_2}}. \tag{19}$$

If $\mathrm{d}x_1 = \mathrm{d}x_2 = 0.5$, the harmonic mean method is recovered, and because the distance effects are considered in this method, a proper name for this method would be "geometric harmonic mean".

3.3. Jump in viscous normal stresses

In the previous section the method to numerically handle the interface shear stress is described. The numerical method for the jump in viscous normal stresses will be discussed in this section. The velocities of the neighboring cells of the interface are used to calculate the jump in viscous normal stresses (as shown in Fig. 2). A local coordinate system is set up with the interface centroid as the origin, the interface normal as one axis, one edge direction as the second axis, and the cross product of the face normal and the edge direction as the third axis. The distance vectors from the surrounding cells' centers to the interface centroid are represented in this local coordinate system. All the cells' velocities are projected to the interface normal direction. Using Taylor series expansion to first order accuracy for a multivariable function, the interface normal projection of each surrounding cell velocity can be represented as a function of the distance from the cell centroid to the interface center. A 3×3 linear system about the velocities versus the distance vectors is formed in this local coordinate system as

$$u^i_{\mathrm{cf}} = u_{\mathrm{f}} + r^i_{\tau_1} D_{\tau_1} + r^i_{\tau_2} D_{\tau_2} + r^i_n D_n, \tag{20}$$

where u_{f} is the interface normal velocity, u_{cf} denotes the interface normal projection of the cell velocity, $r_{\tau_1}, r_{\tau_2}, r_n$ are distances from the cell center to the interface face centroid in tangential and normal directions

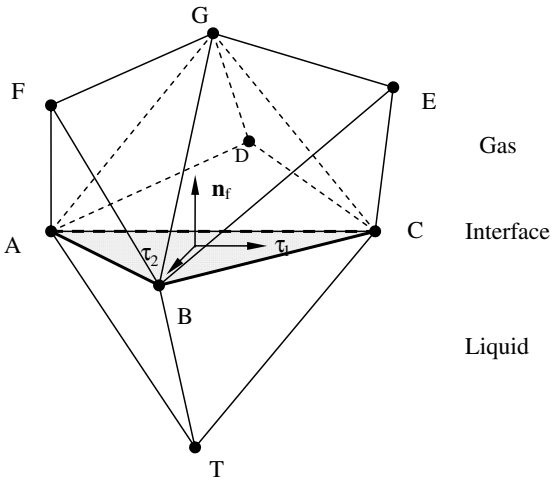

Fig. 2. Interface and surrounding cells.

respectively, D stands for the gradient of the velocity, and the superscript i denotes the cell index with values of 1, 2 and 3. By solving the above 3×3 linear system, the first derivative of the velocity in the face normal direction can be obtained. The same thing can be done on the other side of the interface. Then the jump in the viscous normal stresses across the interface ($\mathrm{JUMP}_{\mathrm{visc}}$) can be calculated by

$$\mathrm{JUMP}_{\mathrm{visc}} = 2.0(\mu_{\mathrm{G}} \cdot D_{\mathrm{G}} - \mu_{\mathrm{L}} \cdot D_{\mathrm{L}}) \cdot A_{\mathrm{f}}, \tag{21}$$

where μ_{G}, D_{G} are the dynamic viscosity and the first derivative of the velocity in gas phase, respectively, while μ_{L}, D_{L} are the corresponding values in liquid phase, and A_{f} is the interface area.

3.4. Stability criteria

The time step is limited by three stability criteria.

(a) CFL (Courant–Friedrichs–Lewy) criterion

$$\Delta t_{\mathrm{cfl}} \leqslant \frac{\mathrm{CFL} \cdot \Delta x}{U}. \tag{22}$$

(b) Surface tension criterion
The surface tension is solved explicitly, so a criterion for surface numerical stability [17] is introduced as

$$\Delta t_{\mathrm{surf}} \leqslant C\sqrt{\frac{\rho \Delta x^3}{2\pi\sigma}}, \tag{23}$$

where the constant C is of order unity and depends on the numerical method.

(c) Mesh Peclet number criterion
The governing equations are solved by forward-time and central difference in the convection term, so the time interval is also limited by the mesh Peclet number criterion, which is

$$2 \cdot \mathrm{CFL} \leqslant Pe \leqslant \frac{2}{\mathrm{CFL}}. \tag{24}$$

This defines a Δt_{Pe} [21].
The time step will be the minimum of the above three time intervals, i.e.

$$\Delta t \leqslant \min(\Delta t_{\mathrm{cfl}}, \Delta t_{\mathrm{surf}}, \Delta t_{Pe}). \tag{25}$$

3.5. Dynamic convergence criteria

The linear system for solving the Navier–Stokes equations is positive semi-definite [22], hence it can be solved by a preconditioned conjugate gradient (CG) method. The convergence criterion for the CG solver can be a function of the norm of unknowns with the current guessed values and the norm of the residuals. One problem with this convergence criterion is that the CG solver will take unnecessary iterations when the guessed values for the unknowns are almost perfect and the magnitudes of the unknowns are also tiny. If the solution is varied with time, which is usually the case, then at some times the convergence criterion is too strict while it is too lax at other times.

A dynamic convergence criterion, which avoids the above problem, is illustrated by a simple case as shown in Fig. 3. The superscript n stands for time step and the subscript m is CG iteration. The convergence tolerance for the current time step is based on the solution change of the previous two time steps, i.e.

$$\mathrm{error\_tot}^n = \mathrm{func}(\Delta X^n) = \mathrm{func}(|X(t^{n-1}) - X(t^{n-2})|) \quad \text{for } n \geqslant 2, \tag{26}$$

where X stands for the vector of unknowns and varies with time. For the case where the unknown is a function of space and time, the error tolerance is

$$\mathrm{error\_tot}^n = \mathrm{func}(|\|\vec{X}(\mathbf{r}, n-1)\| - \|\vec{X}(\mathbf{r}, n-2)\||) \quad \text{for } n \geqslant 2, \tag{27}$$

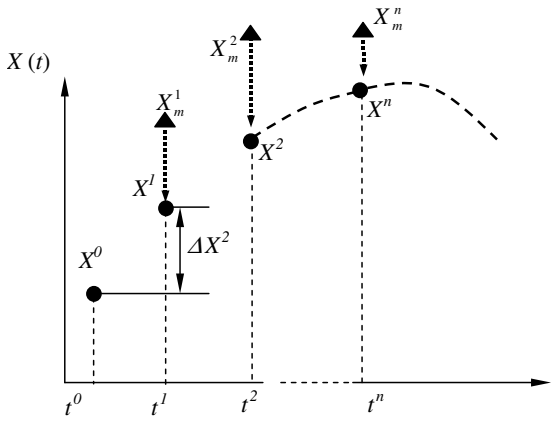

Fig. 3. Dynamic convergence criterion. The superscript n stands for time step, and the subscript m denotes CG iteration. The black dots are the true solutions, and the triangle denotes the solution of each CG iteration.

where $||$ is the absolute value, $\|\|\|$ denotes the norm, and n stands for the time step.

3.6. Surface tension

A least squares parabola fitting in a local coordinate system is used to calculate the effective curvature of the interface. The parabola is fitted in a form of Eq. (28), and the curvature is calculated via Eq. (29). The surface tension is implemented in the pressure boundary condition on the interface. The details of this method are given in [17]

$$z(x,y) = ax^2 + by^2 + cxy + dx + ey + f, \tag{28}$$

$$\frac{1}{R_{\text{effective}}} = -\frac{a(1+e^2) - 2cde + b(1+d^2)}{2(1+d^2+e^2)^{\frac{3}{2}}}. \tag{29}$$

3.7. Periodic boundary condition

In some two-phase flows, a periodic boundary condition is needed, such as a two-layer Couette flow and a droplet in shear flow. In order to implement the periodic boundary condition, identical surface meshes are created initially on the boundaries, which is demonstrated in Fig. 4, where a 2D mesh is shown. Nodes $a, b, \ldots, f$ on the right side of the domain are identical to nodes $A, B, \ldots, F$ on the left side and are offset by the periodic length of the domain along with the edges and faces. The elements (nodes, edges, faces, ghost cells) and their connections on the right side are deleted. The interior elements which are connected to the deleted elements are reconnected to the corresponding elements on the left side. The boundary elements on the left side (except the ones that belong to the upper and lower walls) become interior elements. When using this approach there will be no left side and right side boundaries, and thus the domain is periodic. For example, when nodes (edges) a and b, and face ab of cell abi_1 are deleted, then node i_1 connects nodes A and B respectively, and finally cell abi_1 is replaced by cell ABi_1, and faces ai_1 and bi_1 by Ai_1 and Bi_1, respectively.

4. Mesh adaptations

Edge bisecting, collapsing, and swapping are used together with an optimization-based smoothing method to achieve a good mesh quality for simulating the free-surface flow [17,18]. Special care should be taken for distributing the fluid properties to new cells to avoid mixing phases for interface edge bisecting and collapsing.

As the interface deforms, some interface edges may become extremely long compared to local length scales. The angles opposing these edges may be very large (usually greater than 120°) thus causing poor quality cells

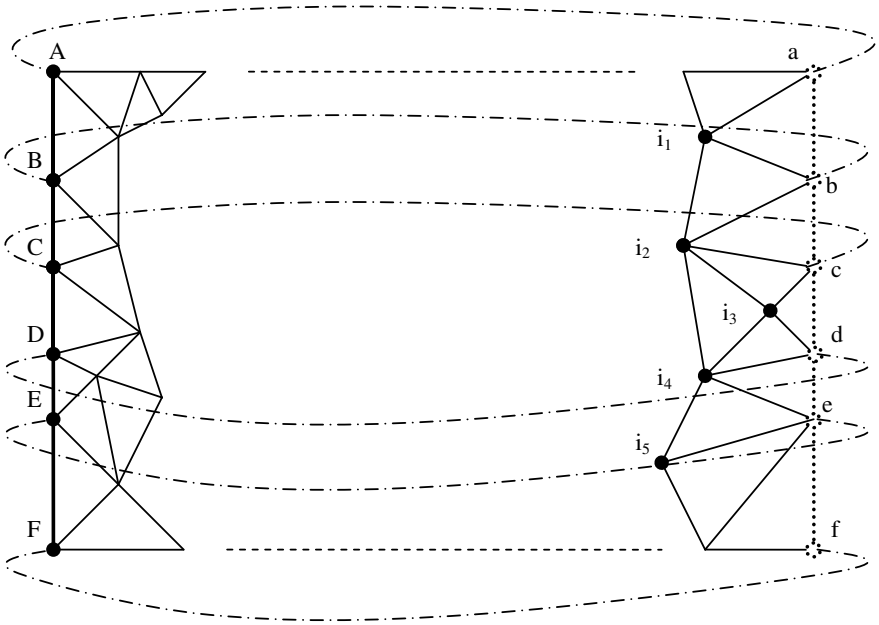

Fig. 4. Schematic representation of the periodic boundary condition. Nodes $a, b, \ldots, f$ on the right side are identical to nodes $A, B, \ldots, F$ and are offset by the periodic distance along with the edges and faces. The boundary elements on the right side are deleted, and then the interior cells with deleted elements are connected to the corresponding elements on the left side.

to appear. Fig. 5(a) shows this situation where angles ADC and ABC are very large and other angles of the two neighboring faces on the interface are very small (usually less than 30°). A 4–4 flipping (as shown in Fig. 5), which disconnects edge AC and then connects node D and B to form a new edge BD, is employed to obtain better mesh quality. The angles of these two faces (as shown in Fig. 5(b)) are now very near to 60°. An equilateral triangle is considered the best quality surface mesh. This flipping is only used for two adjacent faces with a large enough face dihedral angle (usually greater than 170°) in order to conserve mass and preserve

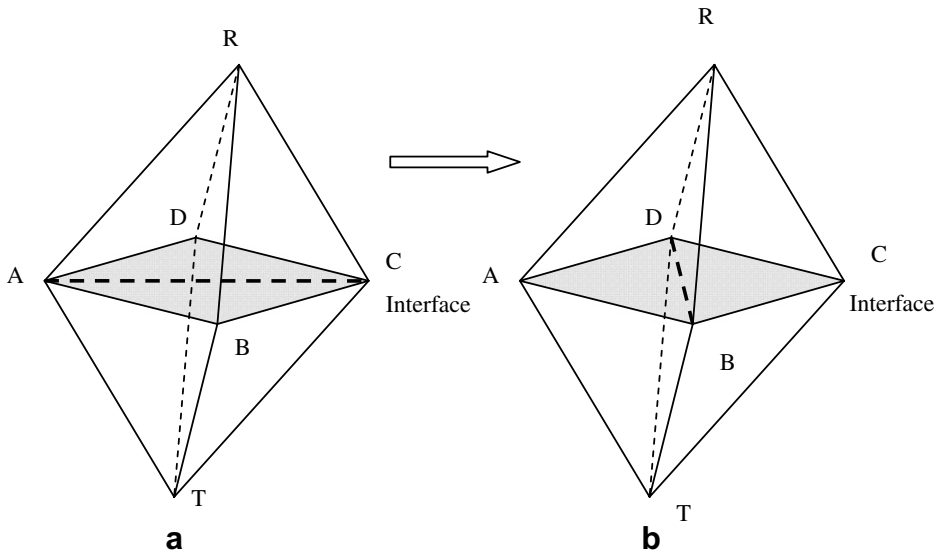

Fig. 5. Sketch of 4–4 flipping. Edge AC is removed and replaced with edge BD to improve the mesh quality. Tetrahedra $ABCT$, $ADCT$, $ABCR$, and $ADCR$ are replaced by tetrahedra $ABDT$, $CBDT$, $ABDR$, and $CBDR$.

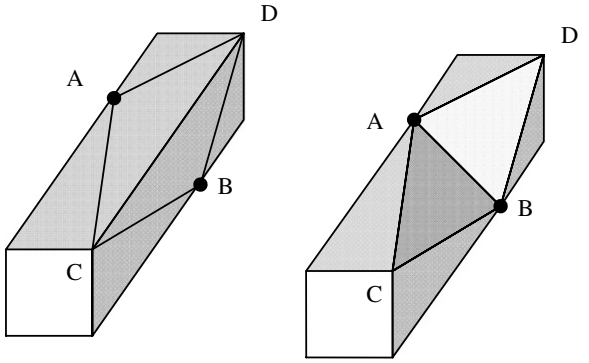

Fig. 6. A case where 4–4 flipping can cause huge mass loss and shape alteration. The dihedral angle between faces *ADC* and *BDC* is 90°.

the interface shape. Fig. 6 shows a case where there is a huge mass loss and interface shape alteration. The face dihedral angle of this case is 90°.

This 4–4 flipping can only be applied to the case where exactly four cells sharing an interface edge with two cells at each phase. Fig. 7 shows a method of edge swapping for an interface edge with more than 4 cells incident. Edge *AB* is bisected first followed by edge contraction on edge *CO* to node *C*. Finally edge *AB* is replaced by edge *CD*, and there are now four cells sharing edge *CD*.

However, some other interface edges may become increasingly short, thus limiting the time step and also causing poor quality cells. Edge contraction is used to improve mesh quality by removing the tiniest edge, but in some cases the edge contraction cannot be done directly. Fig. 8(a) shows a case where no direct edge contraction can be applied to edge *EF* [23]. An indirect way for edge *EF* contraction is shown in Fig. 8(b)–(d), where only faces and edges are shown. Edges *TE* and *TF* are split first, then the edge contractions to node *O*

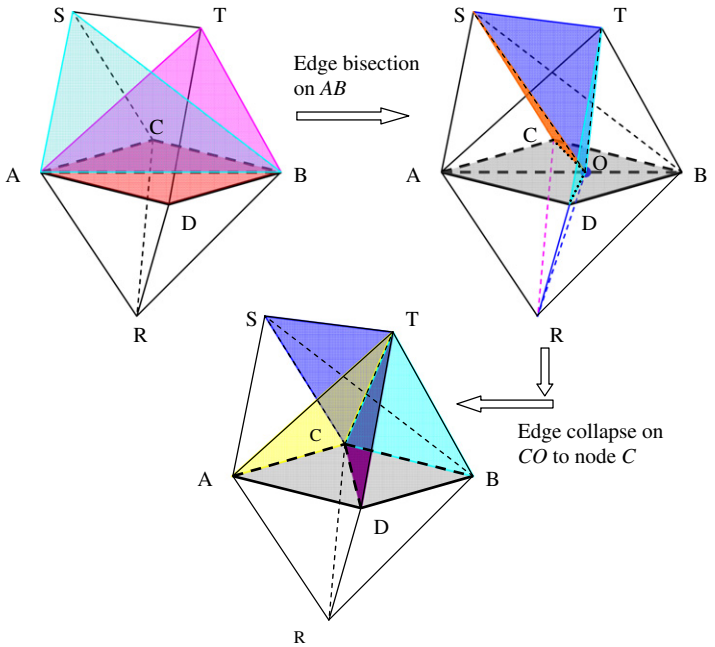

Fig. 7. Edge swapping for the interface edge with more than four surrounding cells. Initially, tetrahedra *ACBS*, *ABST*, *ADBT*, *ACBR*, and *ADBR* are incident to edge *AB*. First, edge *AB* is split by node *O*. The above tetrahedra are split by five new faces *SOC*, *SOT*, *TOD*, *ROD*, and *ROC*. Then, edge *CO* collapses to node *C*. Only four tetrahedra *ADCT*, *BDCT*, *ADCR*, and *BDCR* are incident to edge *CD* after the operations. Tetrahedra *ACST* and *BCST* do not share edge *CD*.

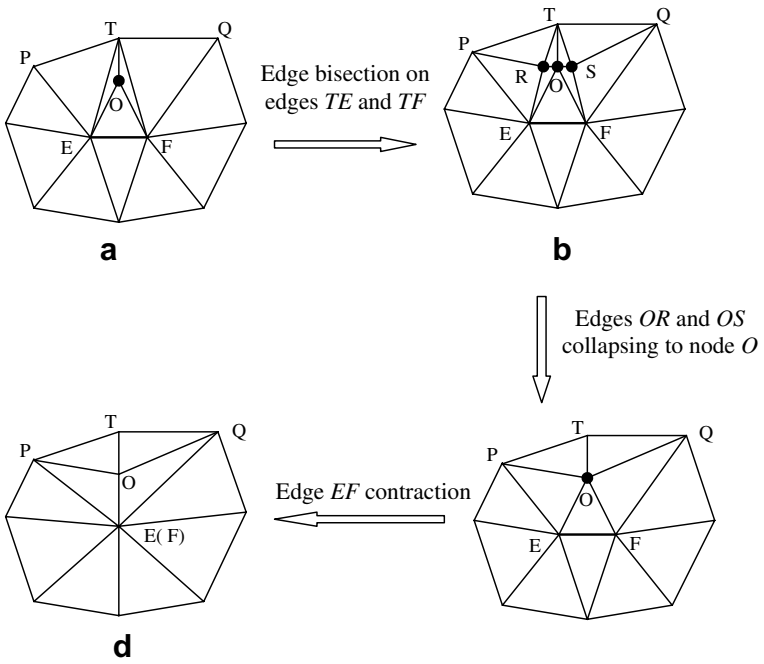

Fig. 8. An indirect way for edge contraction. Only faces are shown, not adjacent cells.

are applied to edges OR and OS, and finally edge EF can collapse successfully. An edge contraction can also be applied to edge OE (F) to improve the mesh quality greatly.

5. Mesh separation

In many multiphase flow applications, such as sprays and ink jets, droplets are formed. In order to handle the topological changes of the cases where the interface breaks, mesh separation is introduced. The cutting position where the neck of the interface will break is usually located by either the physics of the problem or a marker function [24]. This cutting position will be the datum for determining two cutting planes, and the region in between these two cutting planes is defined as the conversion region. In Fig. 9(a), the width of the conversion region is approximately one diameter of the neck region, and two cutting planes are shown. The liquid cells inside the conversion region are converted to gas cells by changing the physical properties of these cells. The liquid cells are shown in gray and gas cells in green in the figure. The elements (faces, edges, nodes) on the two new created interfaces are converted to the interface elements. This conversion can be done by changing their boundary markers. These two new created interfaces are usually not smooth, which can be seen in the right figure of Fig. 9(a). Special treatments on these two interfaces are needed in order to continue numerical simulation. A projection of all nodes on these two new interfaces to local half spheres is performed, and then smoothing and flipping are used to achieve good mesh quality. The new created interface before and after smoothing is shown in Fig. 9(b). The numerical simulation can be restarted from this point. Due to the conversion of liquid cells to gaseous elements, this mesh separation scheme causes mass loss in the liquid phase and mass gain in gas side. The mass error can be kept small by only applying this mesh separation technique to a very thin neck region.

6. Numerical results

Several tests were performed to demonstrate the accuracy and robustness of the scheme. The numerical results are compared with experimental and theoretical solutions. In particular, a two-layer Couette flow, a

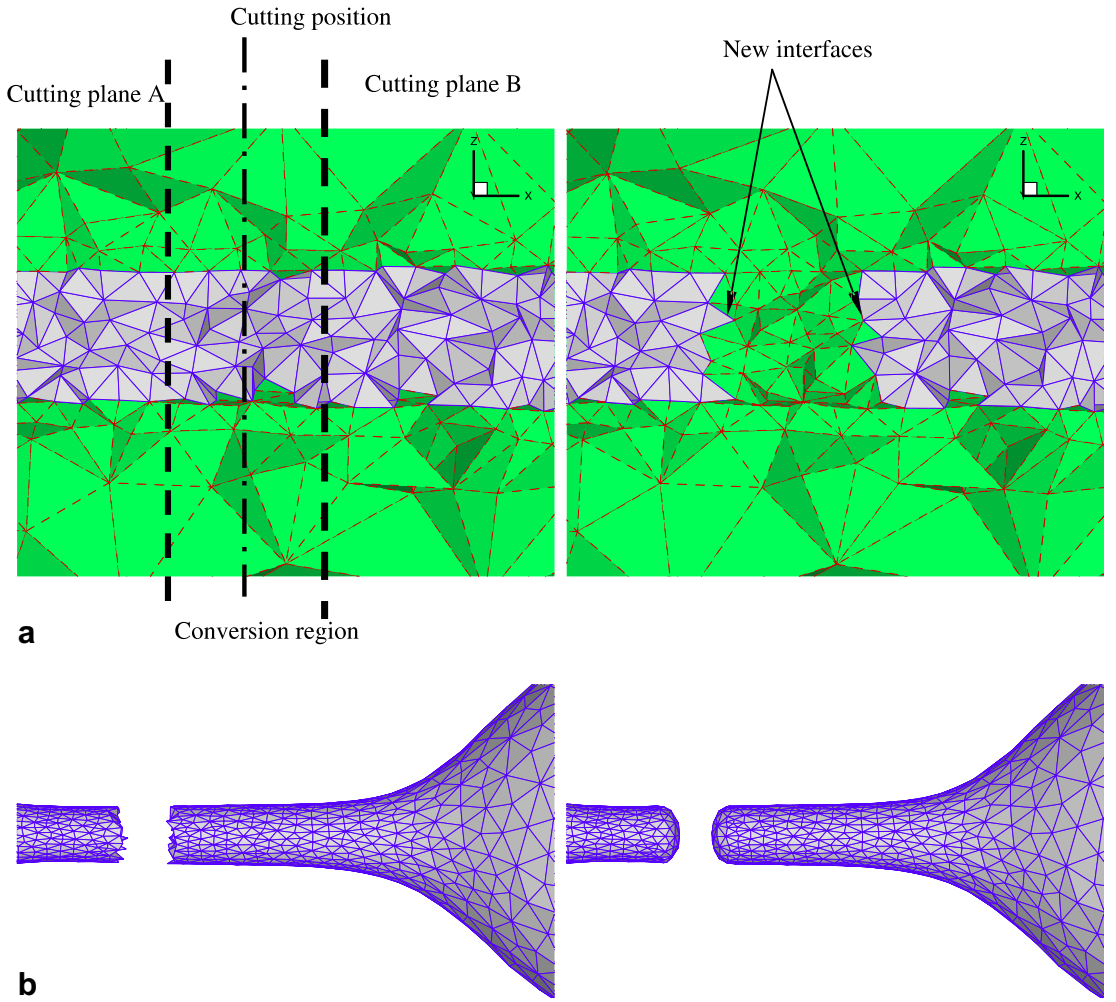

Fig. 9. Mesh separation in two-phase flow. (a) Before and after conversion (gas is shaded in green, liquid in gray). (b) Before and after projection and smoothing (only liquid is shown). (For interpretation of the references in color in this figure legend, the reader is referred to the web version of this article.)

droplet oscillation in a gaseous flow, and a droplet in a shear flow are simulated as tests of accuracy. A ligament end-pinching in a quiescent flow is simulated to illustrate the ability of the scheme to deal with large deformation. A modulated jet pinching off is presented to show the robustness of the method to handle topological transitions.

6.1. Two-layer Couette flow

A three-dimensional, two-layer, incompressible, immiscible Couette fluid flow in a periodic domain (as shown in Fig. 10) is simulated. The geometric harmonic mean method is used for calculating the interface shear stress. The periodic boundary is enforced on the left and right sides of the domain. The upper wall is moving at velocity of U_1 and the lower wall is at rest. The two sides are non-slip walls. The viscosity ratio λ is 0.1 and Reynolds number, which is defined in Eq. (30), is 2.7. The theoretical value of the interface velocity at the steady state is 0.184 m/s, while the numerical simulation predicts the average of the interface velocity of 0.182 m/s. The initial and the steady state velocity profiles are shown in Fig. 11. Here only the velocities on the right side of the domain are displayed for simplicity. The jump of the first derivatives of the velocities is extremely sharp, which can be seen clearly in Fig. 11(b)

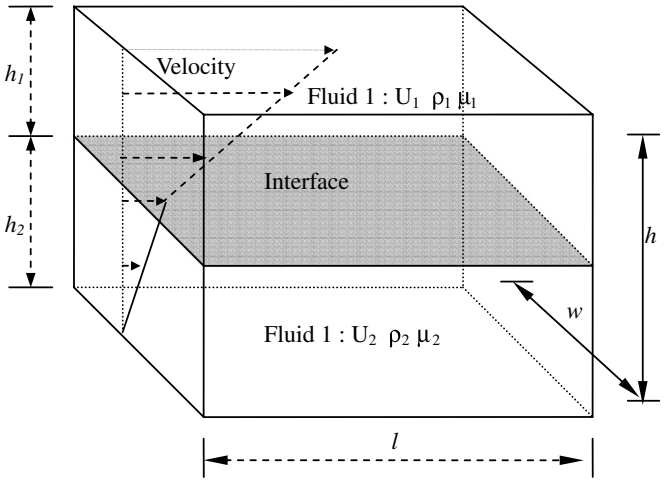

Fig. 10. Sketch of a three-dimensional two-layer Couette flow.

$$Re_1 = \frac{\rho_1(U_1 - U_2)(h_1 + h_2)}{\mu_1}. \tag{30}$$

6.2. Droplet oscillation in gaseous flow

A zero-gravity, three-dimensional droplet oscillation surrounded by gas is computed with $\lambda = 0.01$ and $\eta = \rho_1/\rho_2 = 0.01$. The arithmetic average method is used to evaluate the interface shear stress. The outer gas is fluid 1 and the liquid droplet fluid 2. Unlike Dai et al. [17], the effects of the surrounding gas are considered in this simulation. The initial droplet is a prolate ellipsoid with the major axis 5% longer than the radius of a sphere with an equivalent volume. The viscous droplet experiences a damped oscillation with surface tension as a restoring force. The outer domain is also a sphere and the outer boundary is a slip wall. The Reynolds number based on the maximum velocity and the properties of the liquid is 12.4. The Ohnesorge number based on the liquid properties is 0.013.

The comparison is made between the numerical simulation results and Lamb's analytic solutions in Section 275 and 355 of Lamb [25]. Accordingly, the oscillation period is

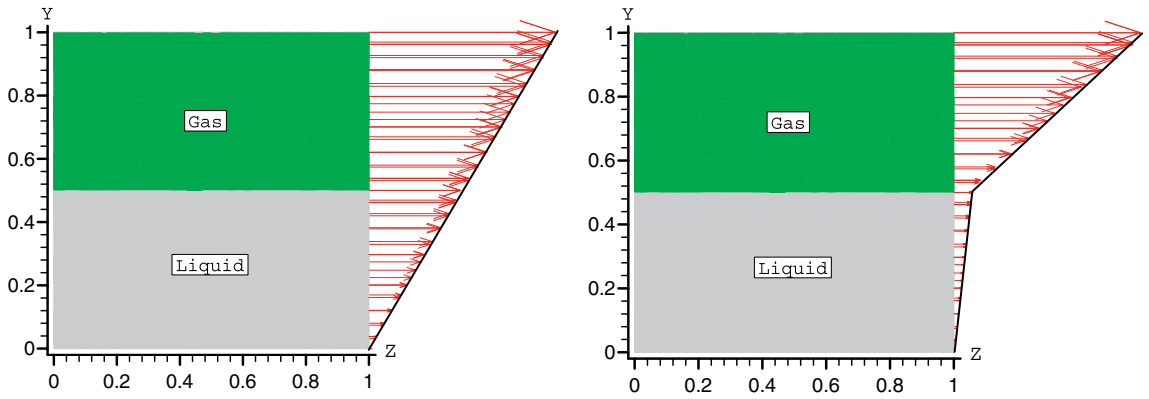

Fig. 11. Velocity distributions for the two-layer Couette flow with $\lambda = \eta = 0.01$. Only the velocities on the right side of the domain are shown. (a) Initial state with linear velocity distribution. (b) Steady state.

$$T = \frac{2\pi}{\sqrt{\frac{n(n+1)(n-1)(n+2)}{(n+1)\rho_2+n\rho_1}\frac{\sigma}{R_0^3}}} \tag{31}$$

and the decay factor is

$$\tau = \frac{R_0^2}{(n-1)(2n+1)\nu_2}, \tag{32}$$

where R_0 is the radius of the spherical drop, ν_2 is the kinematic viscosity of the drop, and n is the oscillation mode number with $n = 2$ being the lowest mode for an incompressible droplet. The numerical results of droplet shape and the velocity field of the whole domain at one quarter period are shown in Fig. 12. The theoretical period and decay factor are 0.2089 s and 1.034, respectively. The numerical results are 0.2108 s and 1.030. The relative errors of the period and decay factor are 0.9% and −0.4%, respectively. Fig. 13 shows the comparison between the theoretical predictions and the numerical results for the droplet oscillation. The numerical results are in good agreement with the theoretical predictions and compare favorably with the previous numerical investigations [26]. The mass conservation of our scheme is shown in Fig. 14, and it is clear that the numerical method causes minimal mass error.

6.3. Droplet under shear

The deformation of a droplet immersed in an immiscible liquid phase, which is a linear shear flow, has been a subject of a number of studies, both theoretically and numerically [27–30]. The dynamics of a droplet in a shear flow can be regarded as a fundamental problem in fluid mechanics, which can provide insights to processes like blending, emulsion and blood flow. Taylor was the first person to theoretically analyze a droplet under shear flow. Small deformation of the droplet is assumed in Taylor's theory. He showed that the deformation factor of the drop is governed by viscosity ratio λ and capillary number Ca, which is defined as

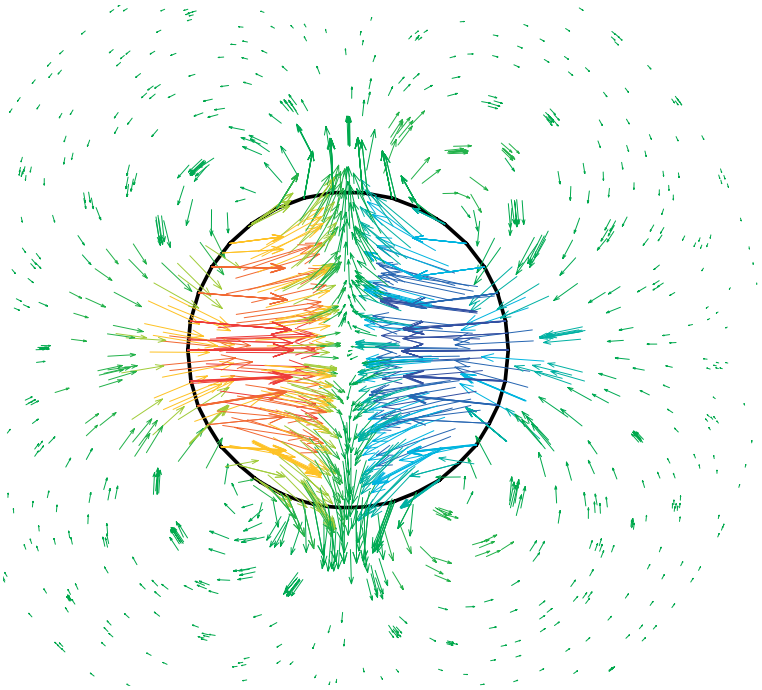

Fig. 12. Oscillating droplet surround by gas with $\lambda = 0.01$ and $\eta = 0.01$. An xy plane slice at a quarter of the period is shown. The black line denotes the droplet shape. The velocities are colored by their x components. (For interpretation of the references in color in this figure legend, the reader is referred to the web version of this article.)

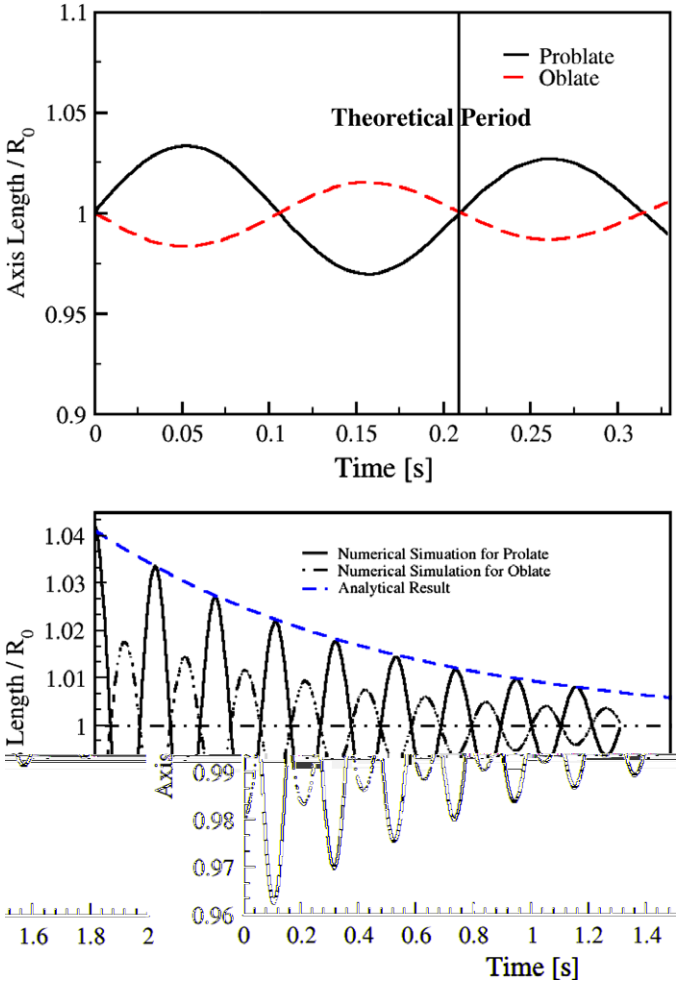

Fig. 13. Period and amplitude decay history of the oscillating droplet with $\lambda = \eta = 0.01$.

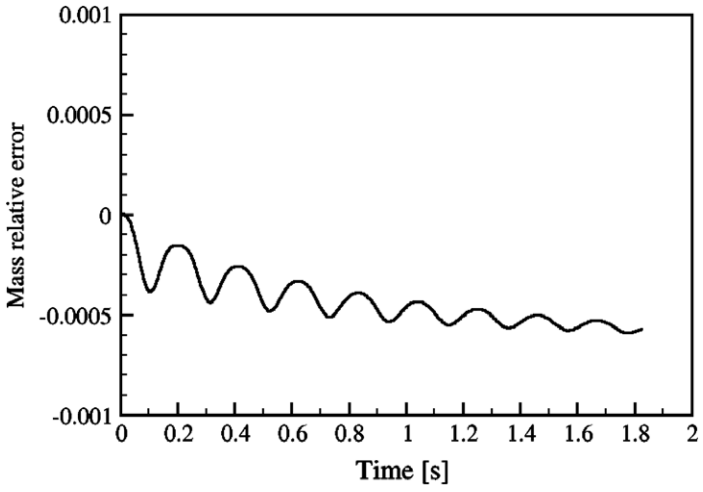

Fig. 14. Mass conservation of the oscillating droplet with $\lambda = 0.01$ and $\eta = 0.01$. The relative error of mass is based on the initial value.

$$Ca = \frac{\mu R_0 \dot{\gamma}}{\sigma}, \tag{33}$$

where R_0 is the radius of the undeformed droplet, $\dot{\gamma}$ stands the shear rate, and σ is the surface tension coefficient between the two immiscible fluids. The deformation factor D is

$$\mathscr{D} = \frac{L - B}{L + B} = Ca \frac{19 + 16\lambda}{16 + 16\lambda}, \tag{34}$$

where L is the longest axis length and B is the shortest axis length of the droplet.

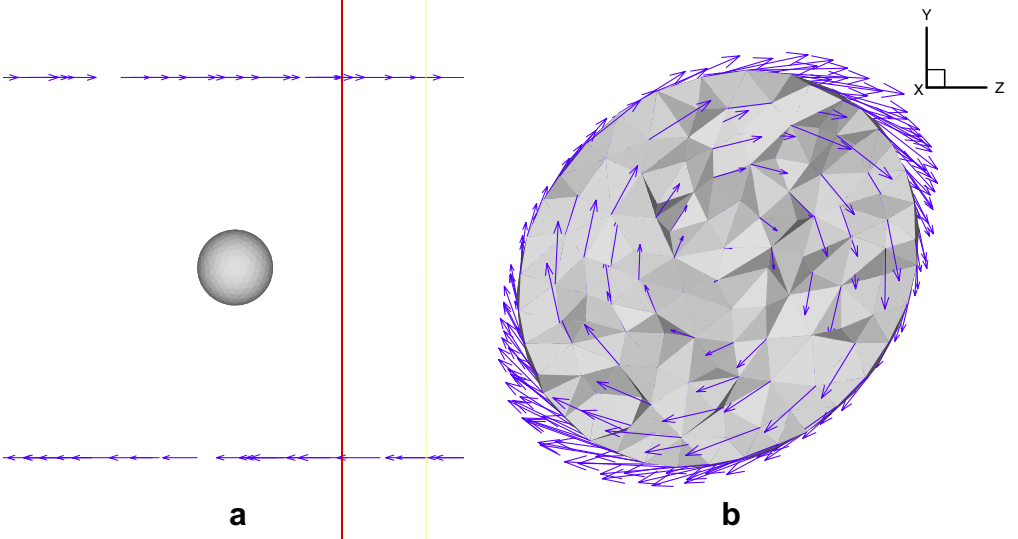

Fig. 15. Droplet under shear. (a) Initial state. Only the upper and lower walls have velocities. The droplet is initially at rest. (b) Steady state. An enlarged view of the droplet and the liquid phase velocities in an xy plane are shown.

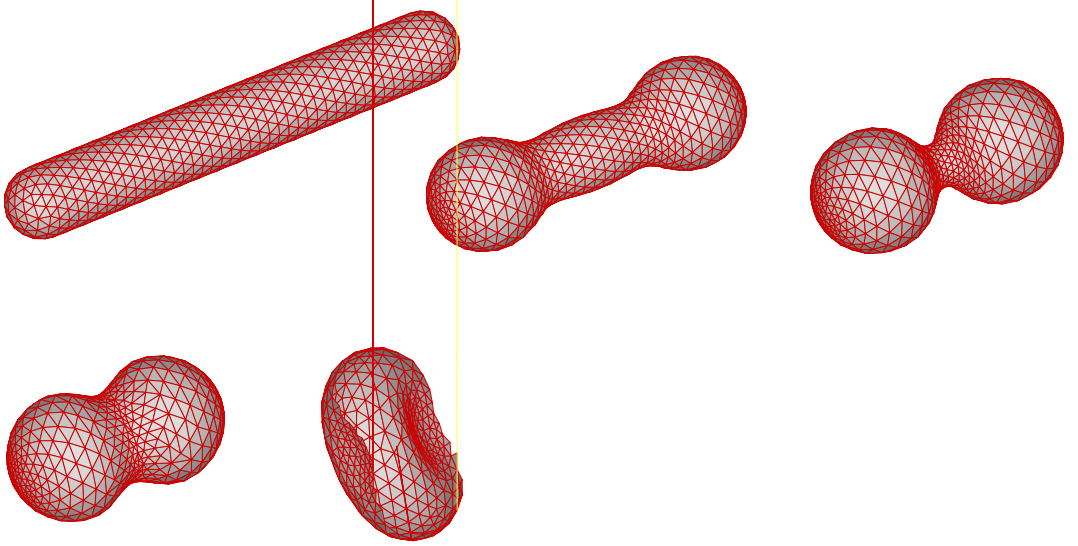

An initially spherical droplet immersed in a shear flow was computed numerically, and the harmonic mean method is used to calculate the interface shear stress. The whole flow field is initially at rest except for the upper and lower walls which have velocities with the same magnitude but opposite direction as shown in Fig. 15(a). The viscosity ratio of the two fluids is 2.0, and the capillary number Ca is 0.05. The deformation factor evaluated by Eq. (34) is 0.053, while Taylor's experimental result [28] gives 0.07. The numerical simulation predicts the deformation factor as 0.076. Fig. 15(b) shows the steady state of the droplet under shear in a yz plane slice with the droplet velocity.

6.4. Ligament end-pinching in a gaseous flow

A ligament collapsing in a gaseous flow is simulated to show the ability of the numerical schemes to handle large deformations. The interface shear stress is evaluated by the arithmetic average method. The flow field is entirely driven by surface tension because the initial flow field is quiescent. The ligament is located in the center of the outer box that is filled with gas. The boundary conditions for the outer box are slip walls. The ligament is 7 diameters in length with the radius R_0 of 0.2 mm. The Ohnesorge number based on the diameter and the suspending fluid is 0.04. The viscosity and density ratios of the two fluids are 0.01. Fig. 16 shows the ligament collapsing at different times. Time is made dimensionless by the time scale $t_c = (1 + \lambda)R_0\mu/\sigma$ (the suspending fluid viscosity is used). The flow field at $t = 55.6$ is given in Fig. 17. There are four vortex rings in the flow field, while no vortex ring was observed in Dai and Schmidt's single phase simulation [18]. The two inner vortex rings result in a neck region. The ligament eventually collapses to a spherical droplet, and its energy is damped out by the viscosities of the two fluids. The viscosity ratio is much greater than unit and the length ratio is small, and this guarantees no breakup in this ligament pinching process [31].

6.5. Modulated jet pinching

Round liquid jets ejecting from a nozzle and flowing into a gaseous environment are very important in a number of industrial applications, such as ink jets. A liquid jet with a nozzle outlet flow velocity that decreases

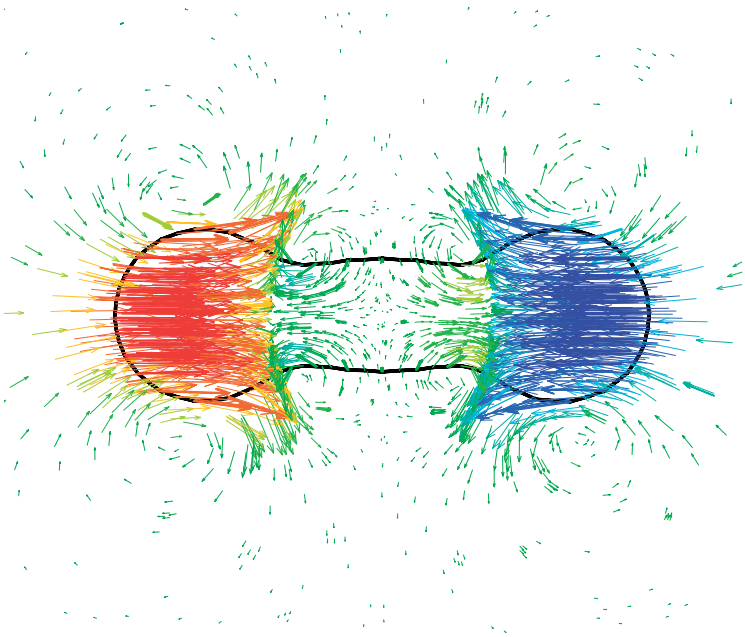

Fig. 17. Flow field of the ligament pinching at $t = 55.6$. An xy plane slice is shown. The black line denotes the interface. The velocities are colored by their axial components. $\lambda = \eta = 0.01$. (For interpretation of the references in color in this figure legend, the reader is referred to the web version of this article.)

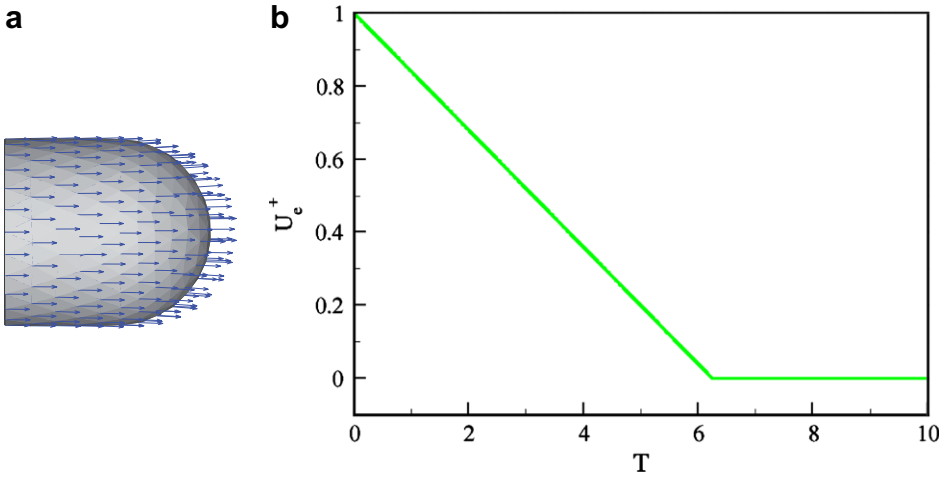

Fig. 18. Modulated jet: (a) initial shape and velocity; (b) nozzle exit velocity versus time.

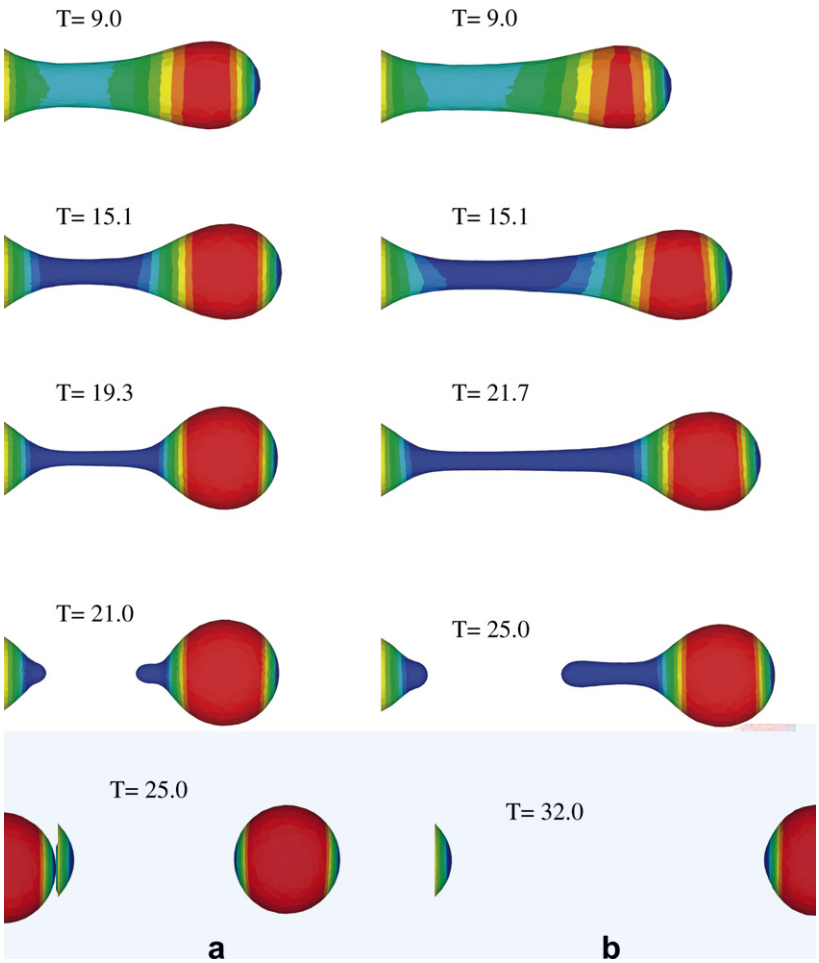

Fig. 19. Formation of a droplet, $\lambda = \eta = 0.02$, colored by radius. (a) $We_i = 12.5$. (b) $We_i = 20.0$. (For interpretation of the references in color in this figure legend, the reader is referred to the web version of this article.)

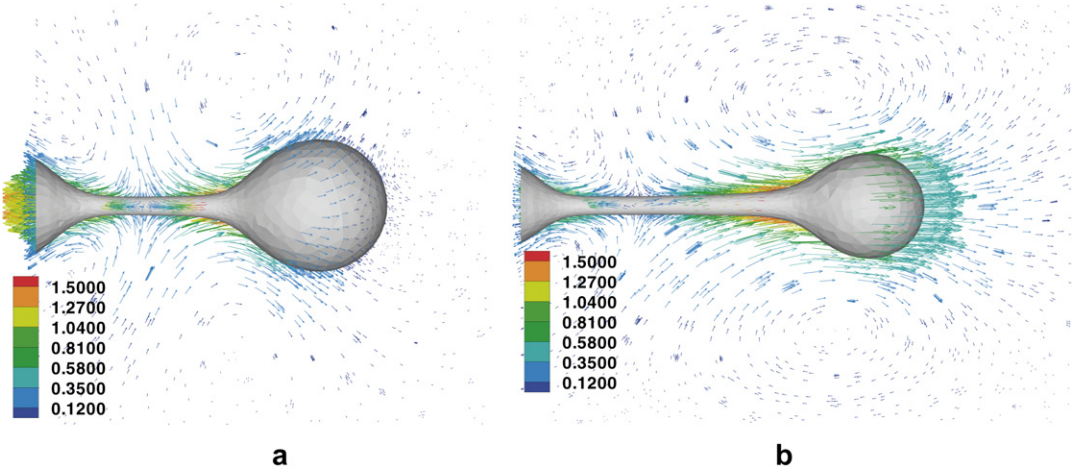

Fig. 20. Velocity profiles of the modulated jets, $\lambda = \eta = 0.02$, colored by velocity magnitude. (a) $We_i = 12.5$, $T = 19.3$. (b) $We_i = 20.0$, $T = 22.6$. (For interpretation of the references in color in this figure legend, the reader is referred to the web version of this article.)

linearly with time is simulated to show the robustness of the methods in handling topological transitions. In this simulation, the harmonic mean method is used to calculate the interface shear stress. Gravity forces are not considered in the simulations. Initially, the liquid jet is a cylinder with a half sphere on its end, and the liquid has a uniform velocity. The length of the cylinder is the same as the radius of the sphere, which is illustrated in Fig. 18(a). The nozzle exit velocity decreases linearly with time as shown in Fig. 18(b). Time is non-dimensionalized by U_e/R_e, where U_e is the nozzle initial exit velocity, and R_e stands for the nozzle exit radius. Two simulations are performed to investigate the effect of surface tension. The viscosity and density ratio of both cases are 0.02. The initial Reynolds number (Re_i) based on the nozzle exit diameter, the initial exit velocity, and liquid properties is 10.0. The initial Weber numbers (We_i) of these two cases are 12.5 and 20.0, respectively. The results from the simulations are shown in Fig. 19. After the nozzle exit velocity becomes zero, there will be a reverse flow on the nozzle exit side due to surface tension while the leading tip will continue its motion due to the momentum. This will lead to a neck region that will become thinner and thinner, until finally the detachment of a droplet will occur.

Because of the low Weber number, the results are sensitive to the value of surface tension. The penetration distance of the case with higher surface tension is much smaller than that of the case with lower surface tension. Also, the frontal area of the jet is smaller for the case with lower surface tension. The velocity profiles of these two cases are illustrated in Fig. 20. It is clear that there are reverse flows on the nozzle exit sides while the jet tips are still moving to the right.

7. Conclusions and discussion

A moving mesh interface tracking method for three-dimensional, incompressible, and immiscible two-phase flow has been developed. In this method the interface is treated as a zero thickness surface and also an internal boundary, so the jump and continuity condition across the interface is implemented directly without any smoothing of the properties of two fluids. The geometric harmonic mean is used for interface viscosity prediction and is second order accurate. The surface tension is calculated explicitly and acts on the interface, which evolves with the fluid. This method conserves mass well, which is shown by the droplet oscillation case. The dynamic convergence criterion, which is based on the change of the previous solutions, makes the simulation efficient. A local adaptive mesh method is used to handle large deformations, and mesh separation is used to deal with topological change. Accuracy of the method is validated against analytical and experimental solutions by several cases. The ligament collapsing case shows the ability of the method to deal with large deformation. The modulated jets show the capability of handling topological changes.

This moving mesh interface tracking method can be used to study the dynamics of a number of interesting two-phase flow problems, such as droplet acceleration/deceleration, deformation, collisions, and secondary breakup in sprays, blood flow, shear instability, etc. The dynamics of a droplet impulsively accelerated by gaseous flow was studied, and some preliminary results were reported in [32]. The modulated jet pinching case starts with 30,000 cells, and due to mesh adaptation to capture the local curvature, the case goes up to 80,000 cells when the neck region develops to a radius of approximately 20% of the initial jet's radius. The calculations take several minutes for one time step on an AMD Athlon MP 2000+ processor. Parallelization can significantly speed up the code and will be addressed in the future.

Acknowledgments

The authors thank Professor Blair Perot at the University of Massachusetts at Amherst for sharing software and hardware resources for this project. The authors also thank Dr. Meizhong Dai for his assistance and advice. This work is funded under ONR contract N00014-02-1-0507 and the NSF Particulate and Multiphase Processes Program.

References

[1] R. Scardovelli, S. Zaleski, Direct numerical simulation of free-surface and interfacial flow, Annual Review of Fluid Mechanics 31 (1999) 567–603.
[2] S. Osher, R.P. Fedkiw, Level set method: an overview and some recent results, Journal of Computational Physics 169 (2001) 463–502.
[3] J.A. Sethian, P. Smereka, Level set methods for fluid interfaces, Annual Review of Fluid Mechanics 35 (2003) 341–372.
[4] G. Tryggvason et al., A front-tracking method for computations of multiphase flow, Journal of Computational Physics 169 (2001) 708–759.
[5] S.O. Unverdi, G. Tryggvason, A front-tracking method for viscous, incompressible, multi-fluid flows, Journal of Computational Physics 100 (1992) 25–37.
[6] C.S. Peskin, Numerical analysis of blood flow in the heart, Journal of Computational Physics 25 (1977) 220.
[7] Z. Li, M.-C. Lai, The immersed interface method for the Navier–Stokes equations with singular forces, Journal of Computational Physics 171 (2001) 822–842.
[8] T.Y. Hou et al., A hybrid method for moving interface problems with application for the Hele–Shaw flow, Journal of Computational Physics 134 (1997) 236–252.
[9] X. He, S. Chen, R. Zhang, A lattice Boltzmann scheme for incompressible multiphase flow and its application in simulation of Rayleigh–Taylor instability, Journal of Computational Physics 152 (1999) 642–663.
[10] T. Inamuro et al., A lattice Boltzmann method for incompressible two-phase flows with large density differences, Journal of Computational Physics 198 (2004) 628–644.
[11] S. Chen, G.D. Doolen, Lattice Boltzmann method for fluid flows, Annual Review of Fluid Mechanics 30 (1998) 329–364.
[12] C. Pozrikidis, Interfacial dynamics for Stokes flow, Journal of Computational Physics 169 (2001) 250–301.
[13] T.Y. Hou, J.S. Lowengrub, M.J. Shelley, Boundary integral methods for multicomponent fluids and multiphase materials, Journal of Computational Physics 169 (2001) 302–362.
[14] S.W.J. Welch, Local simulation of two-phase flows including interface tracking with mass transfer, Journal of Computational Physics 121 (1995) 142–154.
[15] H.H. Hu, N.A. Patankar, M.Y. Zhu, Direct numerical simulations of fluid–solid systems using the arbitrary Lagrangian–Eulerian technique, Journal of Computational Physics 169 (2001) 427–462.
[16] B. Perot, R. Nallapati, A moving unstructured staggered mesh method for the simulation of incompressible free-surface flows, Journal of Computational Physics 184 (2003) 192–214.
[17] M. Dai et al., Direct interface tracking of droplet deformation, Atomization and Sprays 12 (2002) 721–735.
[18] M. Dai, D.P. Schmidt, Adaptive tetrahedral meshing in free-surface flow, Journal of Computational Physics 208 (2005) 228–252.
[19] W. Chang, F. Giraldo, B. Perot, Analysis of an exact fractional step method, Journal of Computational Physics 180 (2002) 183–199.
[20] G. Tryggvason et al. Computations of multiphase flow by a finite difference/front tracking method. 1. Multi-fluid flows, in: 29th Computational Fluid Dynamics: Lecture Series 1998-03. Von Karman Institute for Fluid Dynamics.
[21] J.C. Tannehill, D.A. Anderson, R.H. Pletcher, Computational Fluid Dynamics and Heat Transfer, Taylor & Francis, 1997, p. 792.
[22] M. Dai, Numerical simulation of capillary pinching using an unstructured mesh and finite volume method, MS Thesis, Mechanical and Industrial Engineering, University of Massachusetts, Amherst, 2002, p. 101.
[23] T.K. Dey et al., Topology preserving edge contraction, Publications de I'Institut Mathematique (Beograd) 66 (1999) 23–45.
[24] M. Dai, Numerical Simulation of Free Surface Flow Using a Moving, Unstructured Mesh Method, in MIE, in: MIE, University of Massachusetts Amherst, Amherst, 2005.
[25] H. Lamb, Hydrodynamics, Dover Publications, New York, 1945.
[26] S. Shin, D. Juric, Modeling three-dimensional multiphase flow using a level contour reconstruction method for front tracking without connectivity, Journal of Computational Physics 180 (2002) 427–470.

[27] G.I. Taylor, The viscosity of a fluid containing small drops of another fluid, Proceedings of the Royal Society of London Series A 138 (1932) 41–48.
[28] G.I. Taylor, The formation of emulsions in definable fields of flow, Proceedings of the Royal Society of London Series A 146 (1934) 501–523.
[29] S. Guido, F. Greco, M. Villone, Experimental determination of drop shape in slow steady shear flow, Journal of Colloid and Interface Science 219 (1999) 298–309.
[30] J.M. Rallison, The deformation of small viscous drops and bubbles in shear flows, Annual Review of Fluid Mechanics 16 (1984) 45–66.
[31] H.A. Stone, L.G. Leal, Relaxation and breakup of an initially extended drop in an otherwise quiescent fluid, Journal of Fluid Mechanics 198 (1989) 399–427.
[32] S. Quan, S. Gopalakrishnan, D.P. Schmidt, Effect of droplet distortion on drag coefficient in accelerated flows, in: 19th Annual Conference of ILASS – Americas: Institute for Liquid Atomization and Spray System, Toronto, Canada, 2006.